Vacuum 243 (2026) 114796

Contents lists available at ScienceDirect

Vacuum

journal homepage: www.elsevier.com/locate/vacuum

Evaluation of microstructural evolution of glassy carbon induced by helium implantation and annealing

C.E. Maepa [a,b,*], E.G. Njoroge [a,c], M.Y.A. Ismail [a,d], C. Dickinson [e], Z.A.Y. Abdalla [a], H.A.A. Abdelbagi [a,i], S.S. Ngongo [f], V. Maphiri [g], B.S. Li [h], T.T. Hlatshwayo [a]

[a] Department of Physics, University of Pretoria, Pretoria, 0002, South Africa
[b] Laboratory for Microscopy and Microanalysis, University of Pretoria, South Africa
[c] ENGAGE, University of Pretoria, Pretoria, Pretoria, 0002, South Africa
[d] Department of Physics, University of Zalingei, Zalingei, 63314, Central Darfur, Sudan
[e] JEOL UK, Welwyn Garden City, United Kingdom
[f] Center for High Resolution Transmission Electron Microscopy, Nelson Mandela University, South Africa
[g] Department of Physics, Sefako Makgatho Health Science University, South Africa
[h] State Key Laboratory for Environment-friendly Energy Materials, Southwest University of Science and Technology, Mianyang, Sichuan, 621010, China
[i] Department of physics, University of Zululand, KwaDlangezwa, 3886, South Africa

ARTICLE INFO

Handling Editor: Prof. L.G. Hultman

Keywords:
Glassy carbon
Microstructure
Ion implantation
Ion fluence
Annealing

ABSTRACT

The effects of helium ion (He^{+2}) implantation into glassy carbon (GC) were systematically investigated. He^{+2} ions with an energy range of 17 keV were implanted into GC to fluences of 10^{16}, 10^{17} and 10^{18} cm^{-2} at room temperature (RT). The as-implanted GC samples were subsequently vacuum annealed at 300 °C, 500 °C, and 800 °C for 1 h. Structural evolution of GC was characterized using Raman spectroscopy and transmission electron microscopy (TEM). A fluence-dependent trend in displacement per atom (dpa) and He concentration was observed. Raman spectroscopy revealed progressive structural disorder and amorphization at fluences 10^{17} and 10^{18} cm^{-2}, marked by merging and redshifts of the D and G peaks, indicating tensile strain in the carbon matrix. Partial recovery of D/G peak separation and crystalline order was observed, especially at 800 °C for the 10^{16} cm^{-2} fluence. TEM micrographs showed a confined damaged region of about 130 nm, with distinct defect aggregation towards the bulk for fluences of 10^{16} cm^{-2} and 10^{17} cm^{-2}, whereas the defect aggregation appeared in two regions for the fluences of 10^{18} cm^{-2}. At this high fluence, bubble-like structures were observed upon annealing, indicating He accumulation and pressurisation within the carbon matrix. This observation reveals a nonlinear dispersion and saturation effect. The bubbles contributed to the localized distribution of the lattice structure. Overall, annealing at 800 °C facilitated partial microstructural recovery, particularly for samples implanted to fluences of 10^{16} cm^{-2} and 10^{17} cm^{-2}.

1. Introduction

High electrical energy consumption is a defining characteristic of today's society, with approximately 85 % of global energy still derived from fossil fuels, also known as carbon-based sources. This dependence has led to severe environmental consequences, including global warming, the greenhouse effect, and unsustainable emissions profiles [1,2]. In response, particularly in economically developing countries, nuclear energy has become one of the most efficient low-carbon energy options, capable of significantly reducing global emissions and providing large baseload electricity [2,3]. However, despite its environmental advantages, public concern over nuclear energy remains high, particularly due to the long-lived radioactivity and risks associated with high-level nuclear waste (HLW) [4–6]. One of the key challenges in nuclear technology today is the long-term safe storage of HLW, which needs engineered barriers and materials able to contain radionuclides for extended durations without significant degradation [7]. During the operation of nuclear facilities, radioactive waste dominated by actinides such as uranium (U), plutonium (Pu), and thorium (Th), undergoes alpha decay, continuously emitting helium nuclei (He^{2+}) [8]. These ions are embedded into surrounding materials with well-defined ranges and damage profiles, as predicted by Monte Carlo simulations such as SRIM

* Corresponding author. Department of Physics, University of Pretoria, Pretoria, 0002, South Africa
E-mail address: charity.maepa@up.ac.za (C.E. Maepa).

https://doi.org/10.1016/j.vacuum.2025.114796
Received 11 August 2025; Received in revised form 1 October 2025; Accepted 2 October 2025
Available online 3 October 2025

[9]. Because of their small size, inertness, and high mobility, He^{2+} can migrate through the host lattice, aggregate at defect sites and agglomerate into pressurized helium (He) bubbles. This process is further affected by irradiation-enhanced diffusion and near-surface effects [10]. Unlike previous studies on helium-implanted glassy carbon, which focused on wear properties following implantation with 2 MeV helium at fluences in the range of 10^{15}–10^{17} ions cm^{-2} [11]. The present work provides a comprehensive investigation of helium-induced damage and recovery mechanisms in glassy carbon, offering new insights into its structural resilience and suitability for nuclear waste containment applications.

The thermal conditions within nuclear waste repositories vary significantly depending on waste type, canister design, and host geology. Engineered barriers are typically designed to limit peak temperatures to around 100 °C to prevent material degradation and limit gas release [12,13]. However, in scenarios involving high decay heat from actinide-rich waste or restricted heat dissipation, localized temperatures may exceed 300 °C. In more extreme cases, such as deep borehole storage or dry cask systems, surface temperatures above 500 °C have been predicted [13,14]. These elevated conditions, combined with additional thermal loads such as solar heating, may push surface temperatures of dry storage systems beyond 800 °C [15]. Such extreme conditions can promote chemical reactions, gas pressurisation, and long-term material degradation. Therefore, understanding how candidate barrier materials respond to helium accumulation and thermal stresses across this wide temperature range is essential for designing robust nuclear waste containment systems.

Current interim storage systems, such as dry cask storage, typically depend on sturdy metal containers made from stainless steel, copper, titanium alloys, and nickel-based superalloys [3,7]. These materials are chosen for their mechanical strength and corrosion resistance at ambient and moderately elevated temperatures. However, long-term degradation under combined thermal, chemical, and radiological stresses has revealed their vulnerabilities. For example, copper, while environmentally stable, performs poorly in conditions of brine and radiation exposure due to mechanisms such as sulphide corrosion, gamma radiolysis, and microbial activity [16,17]. Titanium alloys are mechanically strong and corrosion-resistant, but can be susceptible to brittle failure, whereas nickel-based alloys, despite their excellent corrosion resistance, are economically prohibitive [16,18]. Stainless steel offers mechanical integrity alongside corrosion resistance; however, it remains expensive and is vulnerable to catastrophic failure under certain conditions.

As a result, these challenges have prompted the exploration of advanced containment materials. Among these, silicon carbide (SiC) and glassy carbon (GC) have emerged as promising candidates due to their exceptional thermal stability, radiation tolerance, chemical inertness, and impermeability to helium and other fission product gases. SiC has been extensively studied for its performance in nuclear environments, including helium-induced damage evolution [18–20]. However, it exhibits lattice swelling, defect accumulation, and in some cases microcracking, factors that raise concerns about its long-term structural integrity [18,21]. These challenges underscore the necessity of investigating GC, a material characterised by its hybrid structure of nanocrystal graphitic clusters embedded within the amorphous matrix, which imparts resilience to graphitization and inherent defect tolerance. GC, also known as vitreous carbon, is an allotrope of carbon synthesized through high-temperature pyrolysis of polymeric precursors. Unlike other common carbon allotropes, GC has a unique nanoporous structure characterized by short-range crystalline order and a significant presence of defects [21,22]. It exhibits a unique hybrid of glass-like and graphite-like properties, offering excellent thermal stability (up to 3000 °C), chemical inertness, high hardness, and impermeability to gases [23,24]. More recently, its fullerene-like nanostructure and resistance to graphitization have led to increasing interest in its application as a nuclear waste containment barrier, particularly for isolating fission gases [10,18,25,26].

This study aims to investigate the microstructural effects of He^{2+} implantation into GC to fluences of 10^{16} cm^{-2}, 10^{17} cm^{-2} and 10^{18} cm^{-2}, analysing its structural recovery behaviour under vacuum annealing up to 800 °C. These findings provide insights into the suitability of GC as a robust nuclear waste containment barrier under realistic and extreme nuclear storage conditions.

2. Experimental methods

The Sigradur® G GC samples from Hochtemperatur-Werkstoffe (HTW) in Germany were used in this investigation. He^{2+} was implanted into GC to fluences of 10^{16} cm^{-2}, 10^{17} cm^{-2} and 10^{18} cm^{-2} using an energy of 17 keV. The ion implantation was carried out at room temperature. The implanted samples were cut into 10 mm × 5 mm sections using a diamond rotary saw to ensure they fit into the characterization instrument holders. The samples were then successively washed with deionised water and 99.9 % absolute ethanol by ultrasonication for 2 min, repeated three times. Finally, any excess liquid on the surface was removed by blowing with nitrogen gas. The samples were then subjected to sequential vacuum annealing at 300 °C, 500 °C and 800 °C for 1 h, with a controlled heating and cooling rate of 5 °C/min. The process was carried out using the computer-controlled Webb 77 graphite furnace. Characterisation was performed using Raman spectroscopy and TEM to obtain insight into the structural changes.

The Stopping and Range of Ions in Matter (SRIM 2012) simulation code was used to simulate the implantation depth profile, projected range (R_p = 201.6 nm), range straggling (ΔR_p = 50.2 nm), damage in displacement per atom (dpa), and the He^{2+} concentration. The simulation was performed in full damage cascades mode, with a GC density of 1.42 g/cm^3 and displacement energy set to 20 eV.

The WITec Alpha300+ RAS micro-Raman microscope with a 532 nm excitation wavelength was used to monitor the effects of helium ion implantation and subsequent annealing on the microstructure of the GC. The excitation source used in this study was a diode laser coupled with a 100 × objective lens. One of the major drawbacks of Raman spectroscopy is sample heating. To mitigate this, the laser power was kept lower than 1 mW during analysis.

To prepare the samples for TEM analysis, the lamellae were fabricated using an FEI Helios NanoLab DualBeam 650 focused ion beam (FIB) system. A carbon protective layer was deposited on the surface to protect the GC. Thinning of the lamellae was performed using a 30 keV gallium ion beam, with the final polishing performed using the 5 eV and 2 keV Ga ions to further produce near-damage-free TEM lamellae. The samples were analysed using a JEOL JEM 2100 LaB6 Transmission electron microscope in bright field mode.

3. Results and discussion

As shown in Fig. 1(a), the dpa increases with fluence, reaching a maximum of about 0.532, 5.32 and 53.2 dpa at fluences of 10^{16}, 10^{17} and 10^{18} cm^{-2}, respectively, with a peak damage depth of about 190 nm from the surface. This fluence-dependent increase in dpa reflects an enhanced probability of defect overlap, agglomeration, and the potential formation of voids or helium bubbles. At this energy range (17 keV), electronic stopping (S_e = 0.082 keV/nm) dominates near the surface at a depth of 10 nm. In contrast, nuclear stopping (S_n = 0.00261 keV/nm) contributes more significantly to vacancy formation deeper into the material at a depth of 200 nm. Since S_n is much lower than S_e, this suggests that the damage created by the He ions in the near surface region of the glassy carbon substrate is due to electronic stopping (ionization). From these results, it is clear that all of the implanted He is embedded in the amorphous region of glassy carbon. The helium ions are initially implanted as He^{2+}, but rapidly neutralize to He^0 (He atoms), which can diffuse through the lattice and become trapped in vacancy clusters, promoting swelling and structural rearrangement. This behaviour is expected, as He atoms, being chemically inert and

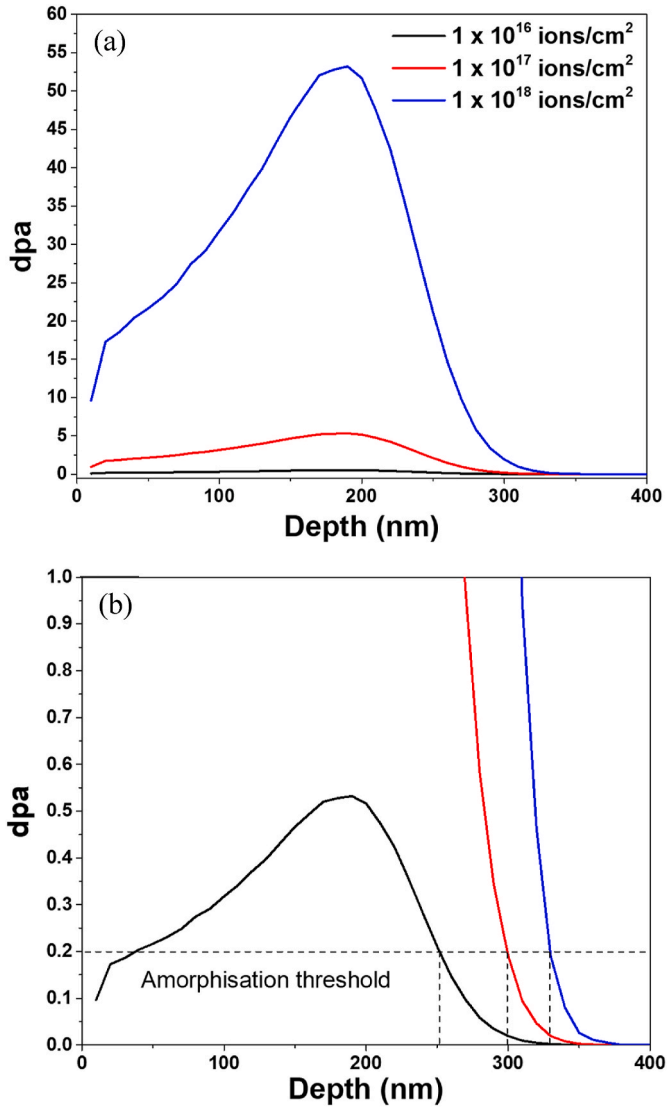

Fig. 1. The SRIM simulation of displacement per atom (dpa) profiles of (a) 17 keV He^{2+} implanted on GC with various fluences of 10^{16} cm^{-2}, 10^{17} cm^{-2} and 10^{18} cm^{-2}, (b) the corresponding magnified region of the dpa profile indicating the amorphization threshold.

significantly smaller than C atoms (with atomic radii of about 0.031 nm and 0.071 nm respectively), exhibit an approximate 1:2 size ratio. Although this ratio suggests that, during nuclear collision, up to two He atoms can occupy a typical C vacancy, the imperfect packing due to the spherical nature and weak interatomic interactions of He results in loosely stacked configurations. Thus, it makes the atoms prone to migration, reordering, or bubble coalescence under thermal or irradiation-induced stress. These collisions contribute to displacement damage and facilitate the trapping of He in vacancy clusters.

The SRIM results also indicate the reported amorphization threshold of about 0.2 dpa for GC (Fig. 1(b)) is attained at all the implantation fluences, which is consistent with the reported dpa range for covalently bonded carbon materials, where complete collapse of structural order is expected to occur [27,28]. This threshold corresponds to different depths depending on fluence. Fig. 1(b) shows that the amorphized region corresponds to depths of about 251.5 nm at 10^{16} cm^{-2}, 299.3 nm at 10^{17} cm^{-2}, and 328.6 nm at 10^{18} cm^{-2}. This represents an increase of approximately 47.8–77.1 nm in amorphization depth with each order of magnitude increase in fluence, suggesting a dependence of amorphization depth on ion fluence, with the amorphization threshold of 0.2 dpa being reached progressively deeper into the material.

Although SRIM provides predictive power, it must be interpreted cautiously. This is because the simulation assumes a homogeneous material and neglects surface roughness, defect agglomeration behaviour, and local structural variations. This is especially relevant for GC, which has a complex hybrid mixture of amorphous and nanocrystalline regions. As shown later in the TEM results, the observed damage region is shallower at about 130 nm than the SRIM prediction of about 200 nm for the highest fluence of 10^{18} cm^{-2}. This discrepancy is attributed to both SRIM's assumptions and the limited visibility of non-agglomerated helium-related defects in TEM due to helium's low atomic number and weak electron scattering.

To further elucidate the microstructural evolution of GC following He^{2+} implantation, Raman spectroscopy with an effective penetration depth of 59 nm was utilized, and the results are shown in Fig. 2. The virgin GC sample exhibited distinct and sharp D (1350 cm^{-1}) and G (1580 cm^{-1}) bands, with minimal overlap, indicating a relatively ordered sp^2 carbon network with some degree of disorder [23]. This observed Raman fingerprint is typical for GC and aligns with previously reported spectra in literature, including that of Ismail et al., who identified sharp D and G peaks as characteristic of partially ordered sp^2 carbon networks [2].

Interestingly, with He^{2+} ion implantation, a progressive broadening and merging of the D and G peaks is observed with increasing fluence. At an implantation fluence of 10^{16} cm^{-2} as shown in Fig. 2, the peaks remain distinguishable, though broader, indicating the onset of radiation-induced disorder. With an increase in the implantation fluence to 10^{17} cm^{-2}, the D and G bands begin to overlap significantly, and at 10^{18} cm^{-2}, the spectrum shows features characteristic of highly disordered or amorphous carbon, a trend consistent with other studies of ion-implanted GC [10,25,26]. This progressive merging of the D and G bands indicates increasing bond distortion, vacancy formation, and structural collapse associated with amorphization. In addition to peak merging, a red shift of the G band, that is, a shift towards lower

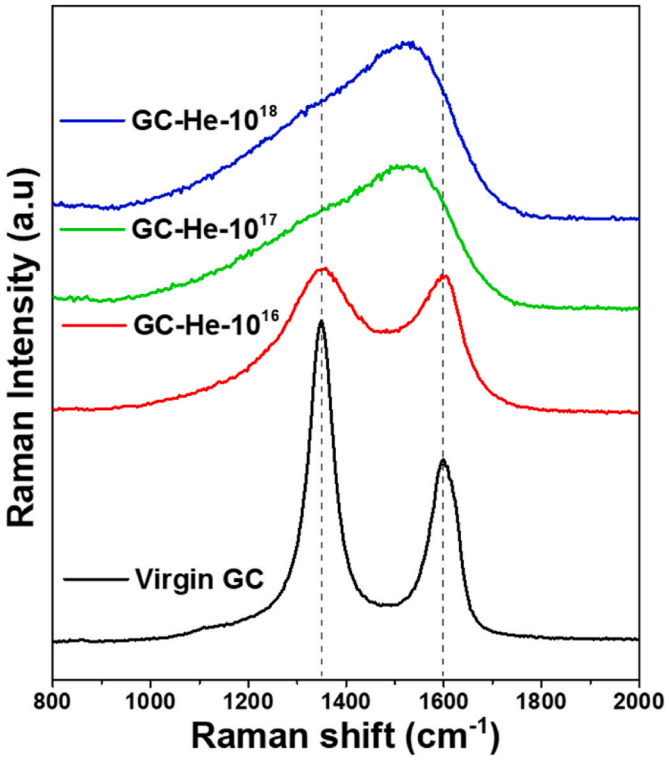

Fig. 2. The Raman spectra of He^{2+} implanted GC at fluences of 10^{16} cm^{-2}, 10^{17} cm^{-2} and 10^{17} cm^{-2}. The spectrum for virgin GC is included for comparison.

wavenumbers, is observed with increasing ion fluence up to 10^{18} cm^{-2}. This shift towards lower wavenumbers (from 1596 cm^{-1} to 1536 cm^{-1}) is commonly attributed to tensile strain in the carbon lattice and an increasing concentration of sp^3-type bonding environments, both of which disrupt the ideal vibrational modes of sp^2 carbon networks [29].

Conversely, the D band remains centred at approximately 1350 cm^{-1} across all fluences, but its full width at half maximum (FWHM) increases significantly as seen in Fig. 3. This broadening without a notable shift suggests that the D band is activated over a wider range of disordered environments, indicative of increased topological disorder rather than strain. It reflects an increasing variability in local bonding environments, where the carbon rings deviate from perfect hexagonal symmetry. This deviation then leads to a broader range of bond angles and vibrational energies, hence the observed D band broadening rather than a simple shift in bond length or force constants [29,30]. Together, the lower wavenumber shift of the G band and the broadening of the D band support a structural transition from nanocrystalline towards amorphous carbon, governed by both lattice strain and increasing defect complexity.

To quantitatively assess the degree of disorder, the intensity ratio (I_D/I_G) was calculated after fitting the Raman spectra using Lorentzian and Briet-Wigner-Fano (BWF) functions for the D and G peaks, respectively. The results are presented in Table 1. Crystallite size (La) was derived using the Tuinstra-Koenig equation, $\left(L_a = C_\lambda / \left(\frac{I_D}{I_G}\right)\right)$ f or cases where$I_D/I_G \geq 1$. Here, C_λ is a laser wavelength-dependent constant, with $C_\lambda = 4.96$ nm for $\lambda = 532$ nm. While the Ferrari-Robertson relation $\left(L_a = \sqrt{\left(\frac{I_D}{I_G}\right)/C_\lambda}\right)$ was applied for $I_D/I_G < 1$ [29]. The I_D/I_G ratio increases with fluence, from 1.8 for the virgin sample to 2.7, 7.7 and 9.2 for 10^{16}, 10^{17}, and 10^{18} cm^{-2}, respectively. This increase reflects a loss of long-range sp^2 ordering and growth in defect concentration [25]. However, the rate of increase in I_D/I_G at the highest fluence suggests a transition to a fully amorphous structure, where the correlation between I_D/I_G and disorder no longer holds. This phenomenon is reported in the late-stage disordering regime of the Ferrari-Robertson model [29].

Table 1
Raman spectroscopy-derived structural parameters for virgin and He^{2+} implanted GC samples.

Sample ID	Amorphous Carbon (%)	Graphitic Carbon (%)	Induced Defect (%)	I_D/I_G	La (nm)	Nature of defects
Virgin GC	5	31	1	1.8	2.8	Few defects
10^{16}	18	17	4	2.7	1.8	Start of major disorder; smaller sp^2 island
10^{17}	23	6	8	7.7	0.6	Highly disordered
10^{18}	23	5	10	9.2	0.5	Maximum damage saturation

To extract more nuanced structural information, the Raman spectra were deconvoluted using a five-peak fitting model, incorporating D, G, D′ (~1620 cm^{-1}), D″ (~1200 cm^{-1}), and I (~1640 cm^{-1}) bands shown in Fig. 3. Lorentzian and BWF functions were applied based on the degree of peak asymmetry and overlap [10,25]. The D″ band is associated with amorphous carbon, the D′ band indicates the presence of nanostructures in virgin GC, and the I band with mixed sp^2-sp^3 bonding environments induced by implantation. At higher fluences, the intensity of the D′, D″, and I bands increases significantly, as shown in Fig. 3, confirming the accumulation of structural defects and the transformation from nanocrystalline to amorphous carbon [10,26]. In heavily damaged spectra, where D and G bands overlapped extensively, BWF fitting was applied exclusively to resolve individual contributions accurately.

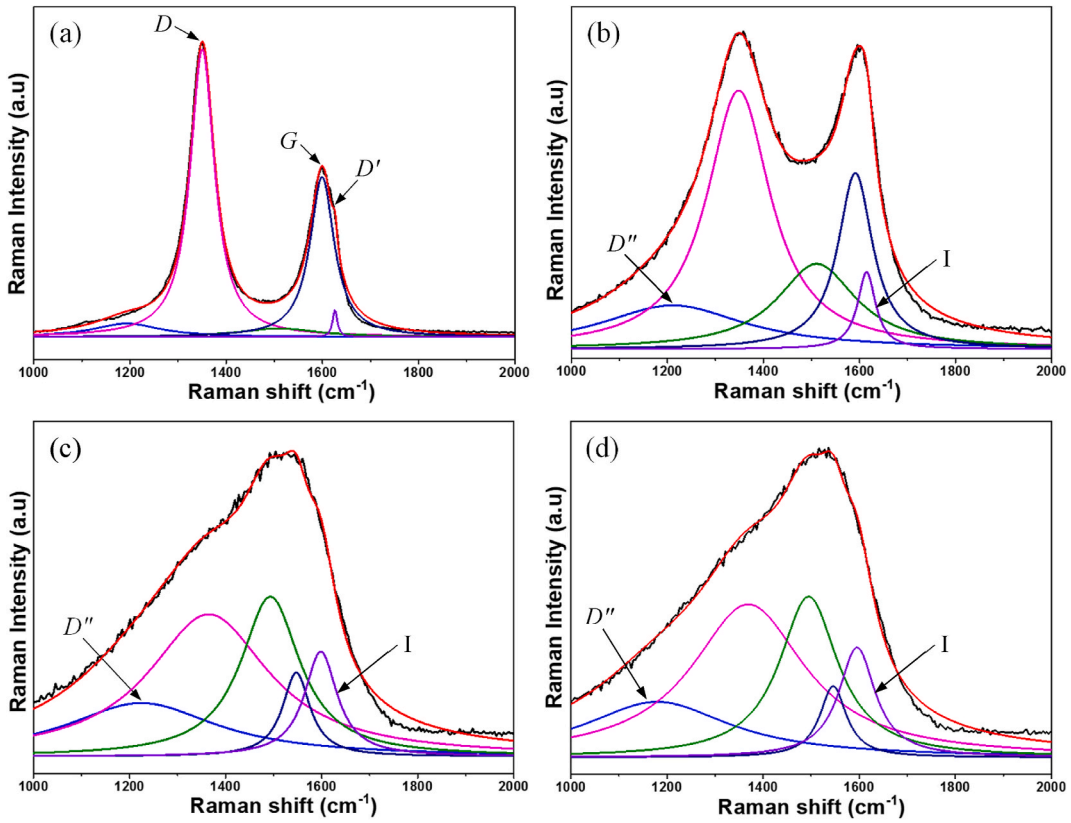

Fig. 3. The Raman spectra fitting spectrum of (a) virgin GC; fitted spectra for GC implanted with He^{2+} to fluences of (b) 10^{16} cm^{-2}, (c) 10^{17} cm^{-2} and (d) 10^{18} cm^{-2}.

The structural evolution and changes in the intensities of the Raman bands with ion fluence confirmed the transition from nanocrystalline to an increasingly disordered or amorphous carbon. Ismail et al. [25] and McCulloch et al. [26] also report similar trends in ion-irradiated GC, where defect-related Raman bands evolve as disorder increases. This observation reflects the fluence-dependent effect localized in the near-surface region.

To further understand the effect of annealing on the He^{2+} implanted GC samples, Fig. 4 shows the Raman spectra of samples annealed at 300 °C, 500 °C and 800 °C. Following the heavily broadened and merged D and G peaks observed in the as-implanted spectra, a progressive spectral recovery is evident with increasing annealing temperature. This is reflected in the gradual separation of the D and G peaks and a relative increase in D and G band intensity, particularly at lower fluences.

Upon annealing at 300 °C, a slight increase in the G peak intensity is observed across all fluences, as shown in Fig. 4(a). This indicates a minor structural modification in the He^{2+} implanted samples. Progressive growth to fluence of 10^{17} cm^{-2} and 10^{18} cm^{-2}, in crystalize sizes (values are not shown here), which occurs at the expense of the D peak. This suggests structural rearrangement in the GC nanocrystals in the samples after annealing at 300 °C. This effect remains modest, particularly for the highest fluence, indicating that low-temperature annealing causes only minimal atomic rearrangement. At higher fluences, partial recovery is evident through the gradual narrowing of peaks and enhanced spectral definition, consistent with the initial stages of crystallite regrowth.

Fig. 4(b) shows the Raman spectra following annealing at 500 °C, revealing a similar trend to that observed at 300 °C, but with more pronounced changes, especially at the highest implantation fluence. The D and G peaks are more clearly resolved at the fluence of 10^{18} cm^{-2}, indicating substantial structural recovery. The reappearance of distinct D and G peaks, where the G peak is dominating, suggests an increase in the size and order of sp^2-bonded domains. At fluence 10^{18} cm^{-2}, a slight shift to higher wavenumbers of the G band is observed with increasing annealing temperature, which is commonly associated with stiffer C-C bond vibrations. This may reflect compressive strain from thermally induced relaxation of the previously disordered matrix.

The effect of annealing at 800 °C is shown in Fig. 4(c). At a lower fluence of 10^{16} cm^{-2}, the most significant structural recovery is observed with the Raman spectra closely resembling that of the virgin GC. A clear separation of the D and G peaks is observed at all fluences following annealing at 800 °C, compared to the lower annealing temperatures. Interestingly, the D and G peak intensities are comparable in the samples implanted to fluences of 10^{17} and 10^{18} cm^{-2}. This suggests comparable levels of structural recovery at these fluences. However, this trend deviates from the expected progression in crystallite growth, indicating a possible variation in the recovery effect at higher fluences, particularly between 10^{17} and 10^{18} cm^{-2}. The continued D peak broadening at 500 °C and 800 °C suggests the persistence of vacancy clusters, voids, or amorphous regions formed during implantation that cannot fully be anneal out.

Overall, the annealing results confirm a fluence and temperature-dependent structural recovery mechanism. While low-fluence samples were partially amorphized (less damage) and thus recovered much of the initial structural order. At high temperature, higher-fluence samples are highly amorphized (more damage) and thus retain signs of residual damage, incomplete restoration and restructuring of the graphitic network being elongated instead of the conventional GC onion rings.

While SRIM simulations were essential for estimating the damage range and Raman spectroscopy provided insight into the bond structure and changes that occurred in the samples, TEM was additionally employed to visualise the microstructural changes, determine the visible damage depth and reveal structural modifications beyond 59 nm. The initial analysis was conducted on a virgin GC to understand the original structure, as shown in Fig. 5(a). The typical GC microstructure is evident in the bright field image with characteristic contrast between dark and bright regions. The dark region suggests scattered electrons, which are a result of the nanocrystals within the material. Whereas the bright spots depict the amorphous regions within the sample, which permit scattered electrons. The high magnification image of this sample is shown in Fig. 5 (a′), exhibiting an onion ring-like structure, where amorphous pockets of an average 5 ± 1.3 nm are encapsulated by approximately six graphitic layers. This is typical, as seen by other authors such as [23].

The TEM micrographs in Fig. 6(a–c) illustrate the microstructural changes induced by He^{2+} implantation. The implantation-affected damaged region is evident across all three fluences, extending from the surface to about 130 nm, which is shallower than the about 200 nm depth predicted by the SRIM simulation. This suggests that some of the voids, defects or damage may be too small to be detected at the resolution of the TEM. This analysis technique is sensitive to features such as defect clusters, nanocrystals, structural rearrangements, amorphous regions and other atomic-scale effects. However, in this case, these features must be sufficiently aggregated or pronounced to be visible. This is challenging, considering the inherently low atomic number of helium,

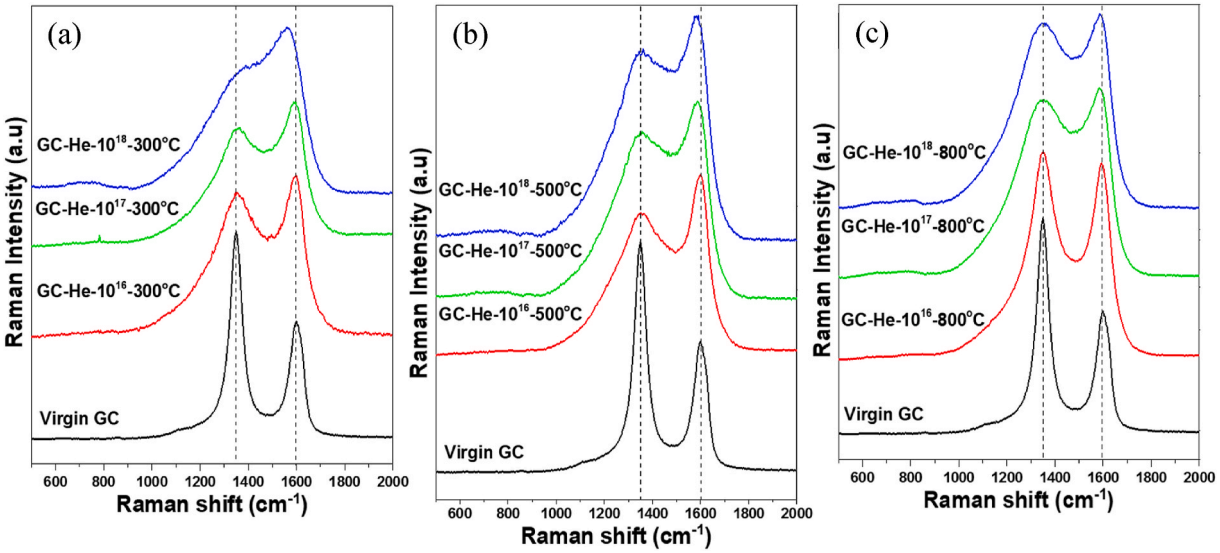

Fig. 4. The Raman spectra of He^{2+} implanted grassy carbon to fluences of 10^{16} cm^{-2}, 10^{17} cm^{-2} and 10^{17} cm^{-2} then annealed at temperatures of (a) 300 °C, (b) 500 °C, and (c) 800 °C. The spectrum for virgin GC is included for comparison.

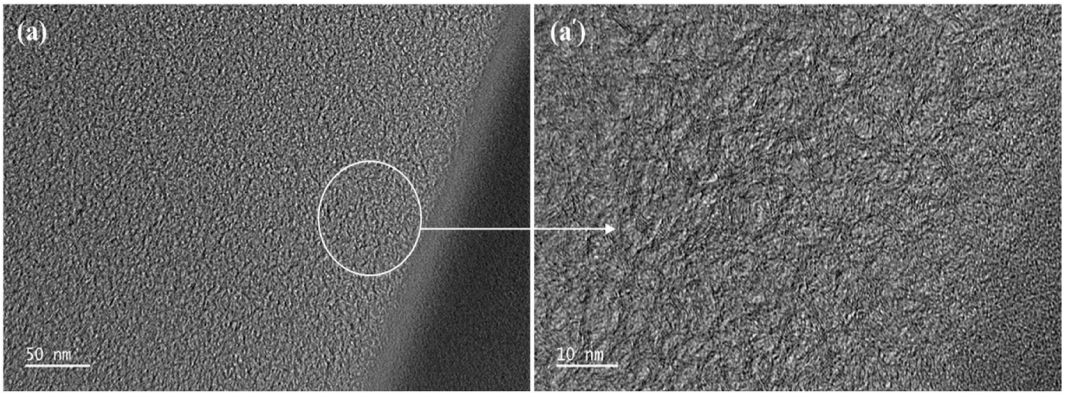

Fig. 5. The TEM bright field micrograph of (a) virgin GC and (a′) the high magnification of the circled area.

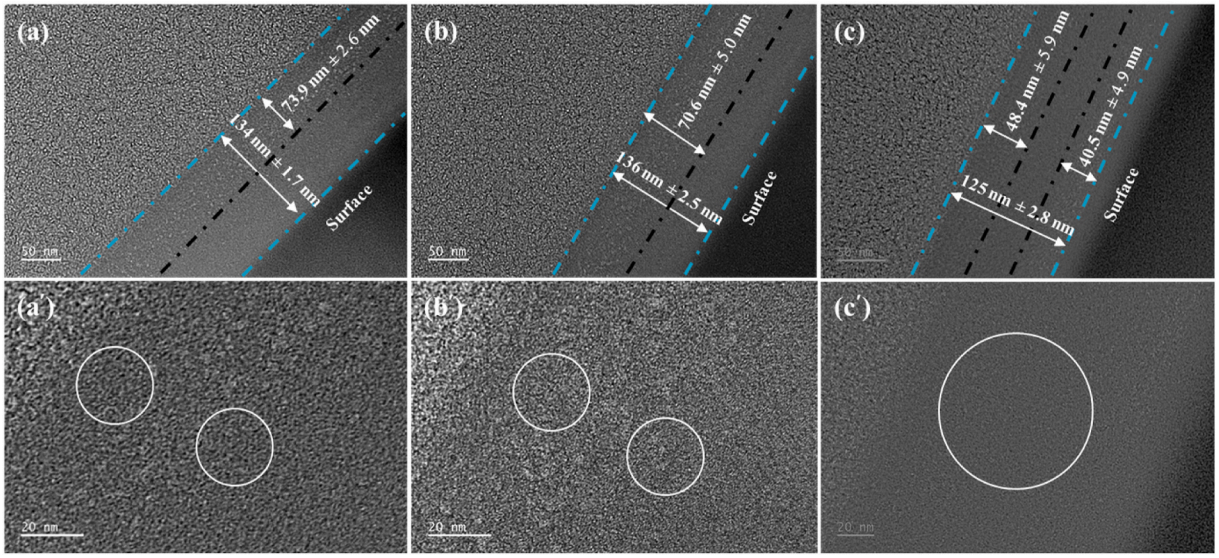

Fig. 6. The TEM micrographs of He^{2+} implanted GC to fluences of (a) 10^{16} cm^{-2}, (b) 10^{17} cm^{-2} and (c) 10^{18} cm^{-2}. The corresponding high magnification images of the damaged region are shown in (a′), (b′) and (c′), respectively.

resulting in minimal contrast and weak scattering. Therefore, it is possible that certain carbon-helium atomic effects (e.g., vacancies) are present but not sufficiently agglomerated to be resolved in the TEM.

In contrast, SRIM may have overestimated the damage since it predicts based on a perfect system that is homogeneously amorphous and may not accurately account for the complex nature of GC, containing both nanocrystals and amorphous regions. Additionally, other factors, such as the surface roughness of the GC or the accumulation/oversaturation of defects, may not be taken into account. Regrettably, the He^{2+} is too small in atomic number; this presents the following challenges: fewer scattering effects, fewer electron emission effects, thus making it undetectable by other complementary techniques such as energy dispersive X-ray spectroscopy and Rutherford backscattering spectrometry, making it challenging to conclude this observation.

The damaged region in the implanted samples exhibits a faint contrast compared to the virgin or the virgin bulk GC, as indicated by the dotted lines in Fig. 6. Within this damaged region, bright spots are observed, suggesting zones with reduced electron scattering. These are proposed to correspond to He bubbles, defect aggregations, or amorphized regions of GC. For this discussion, the bright regions are assumed to be defect aggregates. At lower fluences, these defect aggregates are more concentrated towards the bulk and become more dispersed towards the surface with higher fluences, confirming the fluence dependence effect in the implantation as shown in Fig. 6(a–c).

The gradual aggregation of defects changes as it reaches the highest fluence of 10^{18} cm^{-2}, where it begins to aggregate into two regions, with the additional region appearing towards the surface of the sample. The aggregation regions are smaller, about 40 nm each (due to early stopping in the near-surface tail, and a deeper zone at the projected range peak), compared to the defect's dispersion observed at fluences 10^{16} and 10^{17} cm^{-2}. As saturation is reached, the small size and chemical inertness of He^{2+}, combined with the increasing resistance and elongation of the carbon graphitization, lead to a shift in the damage progression mechanism observed at lower fluences. This nonlinearity was also observed in the Raman spectroscopy discussion.

Fig. 6 (a′-c') is a high magnification of the dispersion defect aggregates. The densities of the darker spots in the GC are highly reduced in the affected regions compared to the bulk area, suggesting fewer nanocrystals or more densely scattering regions in the area. The effect is more pronounced with increasing fluence. Some onion (carbon) rings are stretched open and long as shown in Fig. 6 (a′-c'), compared to the initially observed onion rings in the virgin GC.

To investigate the effect of annealing on the implanted samples, TEM analysis was conducted on the annealed samples at 300 °C, as shown in Fig. 7(a–c). In the sample implanted to a fluence of 10^{16} cm^{-2}, the implanted region appears slightly darker, with bright spots appearing near the surface. This is consistent with localised variations in electron transparency arising from density gradients. These features may reflect

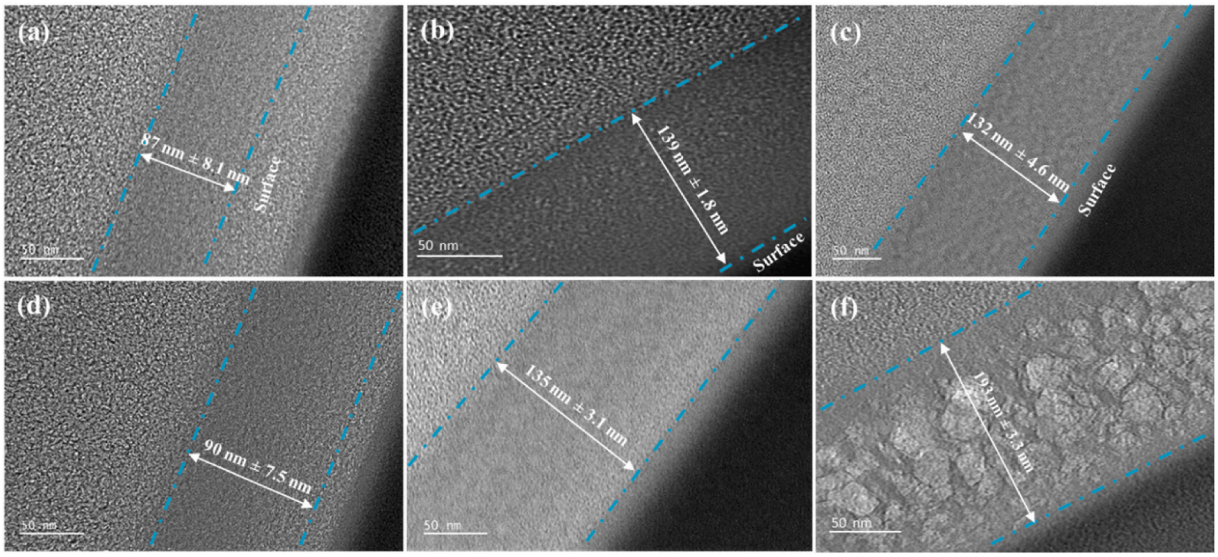

Fig. 7. TEM micrographs of He^{2+} implanted GC annealed at 300 °C to fluences of (a) 10^{16} cm^{-2}, (b) 10^{17} cm^{-2} and (c) 10^{18} cm^{-2}. Corresponding micrographs of the samples annealed at 500 °C are shown in (d), (e), and (f), respectively, for comparison.

early stage nanovoids formation or low-density structural inflation, rather than swelling. The region near the bulk appears slightly out of focus compared to the bulk region, suggesting subtle depth variation or thickness modulation in the damaged region. Furthermore, the reappearance of darker contrast in some regions suggests partial regrowth of nanocrystals, typically associated with dense electron scattering. This effect becomes more pronounced at a fluence of 10^{17} cm^{-2}, correlating with the Raman results that show an increase in the G peak intensity upon annealing. However, at the highest fluence, the morphology shows a bubble increase trend compared to the fluence of 10^{17} cm^{-2}. The defects appear evenly distributed across the damaged region. This may indicate helium clustering or redistribution at high concentration. It is worth noting that the average thickness of this damage region remains about 130 nm.

The effect of increasing the annealing temperature to 500 °C is shown in the micrographs in Fig. 7(d and e). Progressive regrowth of the nanocrystallites and amorphous regions within the damaged region is observed for the sample implanted to a fluence of 10^{16} cm^{-2}. However, this is no longer the case in the sample implanted to a fluence of 10^{17} cm^{-2}, where segregation of the defects occurs, forming larger clusters that exhibit both bright and dark contrast. This effect is more pronounced towards the bulk than near the surface. A complete rearrangement of defects is observed in Fig. 7 (f) for the sample implanted to a fluence of 10^{18} cm^{-2}. The defects increase in size, are randomly shaped, and with aggregates appearing to cluster more toward the middle of the damaged region. Interestingly, an increase in the size of the damaged region is observed at this fluence. This may suggest that the elevated annealing temperature reveals some of the high-fluence defects that were not resolved at lower temperatures. Secondly, there is migration of the unresolved smaller helium bubbles from the bulk towards the centre. The defect aggregates that were previously discussed, which tend to increase at the surface, also appear to form agglomerates that are drawn

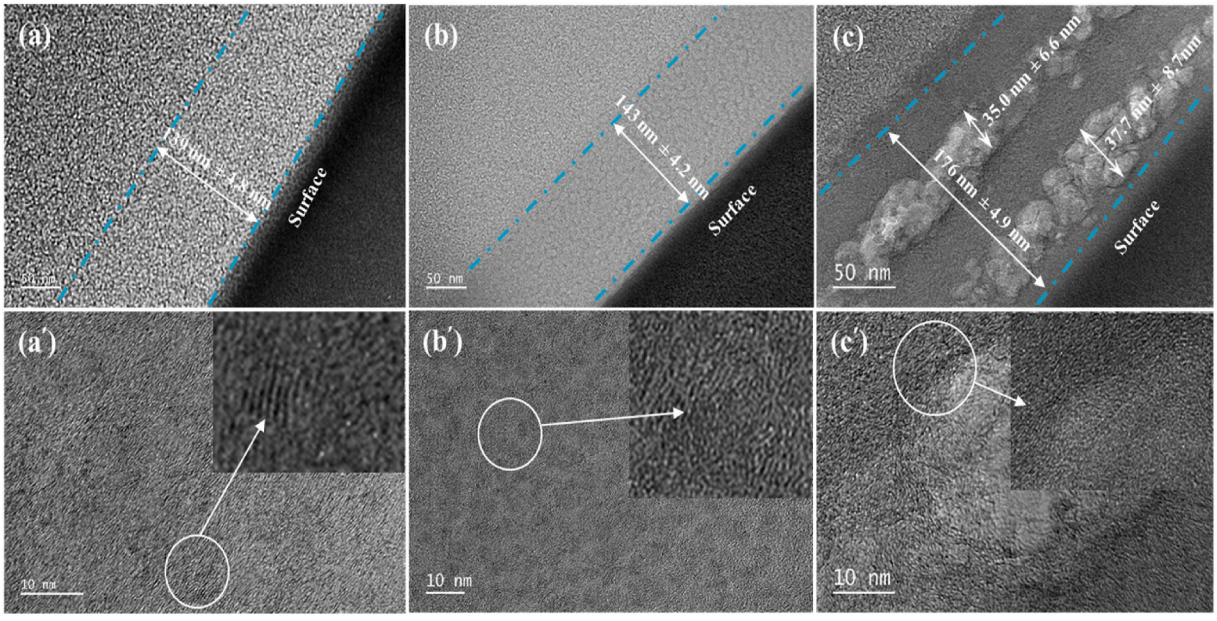

Fig. 8. The TEM micrographs of He^{2+} implanted GC annealed at 800 °C with various fluences of (a) 10^{16} cm^{-2}, (b) 10^{17} cm^{-2} and (c) 10^{18} cm^{-2}. The corresponding high magnification images are shown in (a′), (b′) and (c′) respectively, with the insert representing the higher magnification of the circled areas.

towards the centre.

Fig. 8 shows the TEM micrographs of the samples annealed at 800 °C, where (a-c) show the affected regions for fluences of 10^{16} cm^{-2}, 10^{17} cm^{-2} and 10^{18} cm^{-2}, respectively. The micrographs in (a′-c') represent the high magnification at a scale of 10 nm for the same samples, and the inserts are regions of the images. Starting at a fluence of 10^{16} cm^{-2}, where the damaged region appears only as a faint contrast to the bulk. This indicates close to complete recovery of the GC structure, where the recovery region that was previously observed from the surface has now fully moved towards the bulk.

At a fluence of 10^{17} $cm^{-2,}$ segregation of smaller bubbles and defect agglomerates is observed. These defects are almost spherical in shape and average about 10 nm in size. This seems to complete the morphology observed at 500 °C. Interestingly, the agglomerate is uniformly dispersed across the affected region, and the high magnification shows that the aggregates house pockets of dense regions, which are further surrounded by the carbon chains and further surrounded by amorphous regions.

At a fluence of 10^{18} cm^{-2}, diffusion, coalescence, and stress-driven alignment transform bubbles into two distinct regions. He mobility is high enough to drive clustering into the two He-rich zones. Consequentially, stress in the GC matrix promotes alignment of the defected onion-ring like structure, flatten into elongated, interconnected planar defects, acting like a barrier. These defect at shallow region traps near-surface bubbles, while the deeper defects traps projected range accumulation.

As previously discussed, some onion graphitic rings are stretched open and long, compared to the initially observed onion rings in the virgin GC.

The transformation of the onion-like graphitic rings in virgin GC into elongated rings forces the He bubbles into regions (see Fig. 8(c′)). Additionally, as seen in the figure, elongated graphitic rings alongside the bubbles are observed. This may be attributed to GC forcing the He bubbles to escape from the original vacancy and agglomerate, leading to bubble expansion, leading to overall lattice swelling [31]. Saturation may have contributed to this observation. It is also worth noting the expansion of the damaged region width with increasing temperature (at 800 °C), further confirming lattice swelling due to annealing. The high magnification micrograph shows that even with the increase in dense nanocrystals, longer carbon ring chains persist. This further supports the regrowth of the G peak observed in the Raman spectroscopy discussion. However, the observed minimum disorder peak could be attributed to the limited laser penetration depth of 59 nm, which may not have probed the precise region where the bubble region resides.

4. Conclusion

This study systematically evaluated the microstructural evolution of glassy carbon (GC) under helium implantation and subsequent annealing, with particular emphasis on its relevance for nuclear waste containment applications. The combined SRIM simulations, Raman spectroscopy, and TEM analyses revealed a fluence- and temperature-dependent interplay between disordering, defect aggregation, and recovery mechanisms. At implantation fluences up to 10^{17} cm^{-2}, GC exhibited progressive amorphization, lattice strain, and nanocrystalline distortion, whereas the highest fluence of 10^{18} cm^{-2} induced saturation effects manifested as nonlinear defect accumulation, two-region aggregation, and bubble-like structures. These features underscore the transition from isolated defect clusters to helium bubble pressurisation and coalescence at extreme ion fluences.

Annealing studies demonstrated that thermal treatment up to 800 °C facilitated partial structural recovery, particularly at low and intermediate fluences, restoring D/G peak separation in Raman spectra and enhancing nanocrystalline regrowth in TEM micrographs. However, at the highest fluence, residual disorder and bubble-induced heterogeneity persisted, highlighting intrinsic limitations in fully reversing irradiation damage once helium oversaturation is achieved. The observations of tensile-to-compressive strain transitions, defect redistribution, and agglomeration with annealing further underline the complex thermodynamic and kinetic processes governing helium behaviour in GC.

Overall, the results confirm the exceptional radiation tolerance and thermal stability of GC, with significant recovery achievable under high-temperature annealing conditions. Nonetheless, the persistence of bubble-like structures at extreme fluences suggests that helium accumulation and nonlinear dispersion effects may impose long-term challenges for its deployment in severe nuclear storage environments. These findings provide critical insights.

CRediT authorship contribution statement

C.E. Maepa: Writing – original draft, Methodology, Conceptualization. **E.G. Njoroge:** Writing – review & editing, Supervision. **M.Y.A. Ismail:** Writing – review & editing, Supervision, Investigation. **C. Dickinson:** Writing – review & editing, Supervision. **Z.A.Y. Abdalla:** Writing – review & editing, Visualization. **H.A.A. Abdelbagi:** Writing – review & editing, Visualization. **S.S. Ngongo:** Investigation. **V. Maphiri:** Writing – review & editing, Investigation. **B.S. Li:** Writing – review & editing, Resources. **T.T. Hlatshwayo:** Writing – review & editing, Supervision, Resources, Investigation.

Declaration of competing interest

The authors declare that they have no known competing financial interests or personal relationships that could have appeared to influence the work reported in this paper.

Acknowledgement

Financial support from the University of Pretoria (Laboratory for Microscopy and Microanalysis) and the National Research Foundation of South Africa (Grant number: 2204072593) is gratefully acknowledged.

Data availability

Data will be made available on request.

References

[1] A. De B, P. Peduzzi, S. Kluser, G. Giuliani, in: Environment Alert Bulletin vol. 2, UNEP, Europe, 2004, p. 4.
[2] M.Y.A. Ismail, Z.A.Y. Abdalla, E.G. Njoroge, O.S. Odutemowo, J.B. Malherbe, T. T. Hlatshwayo, E. Wendler, J. Aftab, H. Younis, Investigating structural changes and surface modification in glassy carbon induced by xenon ion implantation and heat treatment, Nuclear Instruments Methods in Physics B 522 (2022) 38–46.
[3] International Atomic Energy Agency, Storage of Radioactive Waste, IAEA Safety Standards Series No. WS-G-6.1, IAEA, Vienna, 2006.
[4] H. Krause, Disposal of radioactive wastes, Naturwissenschaften 59 (9) (1972) 412–417.
[5] U.S. Nuclear Regulatory Commission, Dry Cask Storage of Spent Nuclear Fuel, NRC, USA, 2013.
[6] H.J. Matzke, Radiation damage in nuclear materials, Nuclear Instruments Methods in Physics B 65 (1 – 4) (1992) 30–39.
[7] M. Yim, K.L. Murty, Materials issues in nuclear-waste management, the Journal of the minerals, Metals & Materials Society 52 (2000) 26–29.
[8] J.K. Shultis, R.E. Faw, Fundamentals of Nuclear Science and Engineering, first ed., CRC Press, 2002 https://doi.org/10.1201/9780203910351.
[9] J. Ziegler, SRIM 2012 computer code. www.srim.org, 2012.
[10] J.D. Arregui-Mena, T. Koyanagi, D.A. Cullen, M.J. Zachman, Y.-R. Lin, P. D. Edmondson, Y. Katoh, Comprehensive characterisation of the irradiation effects of glassy carbon, Acta Mater. 281 (2024) 120441.
[11] John T.A. Pollock, Matthew Farrelly, Leszek S. Wielunski, Wear of ion implanted glassy carbon, Mater. Res. Soc. Symp. Proc. 93 (1987).
[12] OECD, Methods for Safety Assessment of Geological Disposal Facilities for Radioactive Waste: Outcomes of the NEA MeSA Initiative, 2012.
[13] U. Maurer-Rurack, G. Bracke, E. Hartwig-Thurat, A. Meleshyn, Torben Weyand, On the temperature in a final disposal site for high-level radioactive waste, Saf. Nucl. Waste Disposal 1 (2021) 99–100.

[14] J. Li, Yun Y. Liu, Thermal modelling of a vertical dry storage cask for used nuclear fuel, Nucl. Eng. Des. 301 (2016) 74–88.
[15] S. Jorge, G. Zigh, Impact of variation in environmental conditions on the thermal performance of dry storage casks, U.S, Nuclear Regulatory Commission, Office of Nuclear Material Safety and Safeguards, NUREG-2174 (2016) 1–44.
[16] L. Werme, P. Sellin, N. Kjellbert, Copper canisters for nuclear high level waste disposal. Corrosion Aspects, Swedish Nuclear Fuel and Waste Management Co, 1992.
[17] D.S. Hall, M. Behazin, W.J. Binns, P.G. Keech, An evaluation of corrosion processes affecting copper-coated nuclear waste containers in a deep geological repository, Prog. Mater. Sci. 118 (2021) 100766.
[18] M.Y.A. Ismail, Z.A.Y. Abdalla, E.G. Njoroge, T.T. Hlatshwayo, J.B. Malherbe, A. J. Innocent, Huzifa M.A.M. Elnour, Study of the effect of implantation temperature on the migration behaviour of Xe implanted into glassy carbon, Appl. Radiat. Isot. 206 (2024) 111239.
[19] T.T. Hlatshwayo, C.E. Maepa, M. Msimanga, M. Mlambo, E.G. Njoroge, V. A. Skuratov, S.V. Motloung, J.B. Malherbe, Helium assisted migration of silver implanted into SiC, Vacuum 183 (2021) 109865.
[20] T. Mokgadia, Z. Abdalla, H. Abdelbagi, M. Msimanga, C. Maepa, V. Skuratov, T. Hlatshwayo, Helium and strontium co-implantation into SiC at room temperature and isochronal annealing: structural evolution of SiC and migration behaviour of strontium, Mater. Chem. Phys. 294 (2023) 126998.
[21] S.J. Zinkle, L.L. Snead, Designing radiation resistance in materials for fusion energy, Annu. Rev. Mater. Res. 44 (2014) 241–267.
[22] M.Y.A. Ismail, The Migration Behaviour of Xenon Implanted into Glassy Carbon, University of Pretoria, 2019. PhD Thesis.
[23] H.O. Pierson, Handbook of Carbon, Graphite, Diamond and Fullerenes: Properties, Processing and Applications, Noyes Publications, New Jersey, 1993.
[24] J.B. Malherbe, O.S. Odutemowo, E.G. Njoroge, D.F. Langa, T.T. Hlatshwayo, C. C. Theron, Ion bombardment of glassy carbon, Vacuum 149 (2018) 19–22.
[25] M.Y.A. Ismail, Z.A.Y. Abdalla, E.G. Njoroge, O.S. Odutemowo, T.T. Hlatshwayo, E. Wendler, V.A. Skuratov, J.B. Malherbe, Effect of high temperature annealing and SHI irradiation on the migration behaviour of Xe implanted into glassy carbon, Nucl. Instrum. Methods Phys. Res. B 489 (2021) 11–19.
[26] D.G. McCulloch, S. Prawer, A. Hoffman, Structural investigation of xenon- ion-beam-irradiated glassy carbon, Phys. Rev. B 50 (1994) 5905–5917.
[27] J.B. Malherbe, P.A. Selyshchev, O.S. Odutemowo, C.C. Theron, E.G. Njoroge, D. F. Langa, T.T. Hlatshwayo, Diffusion of a mono-energetic implanted species with a Gaussian profile, Nucl. Instrum. Methods Phys. Res. 406 (2017) 708–713.
[28] H. Gnaser, Low-Energy Ion Irradiation of Solid Surfaces, Springer, Germany, 1999.
[29] A.C. Ferrari, J. Robertson, Interpretation of Raman spectra of disordered and amorphous carbon, Phys. Rev. B 61 (2000) 14095–14107.
[30] F. Tuinstra, J.L. Koenig, Raman spectrum of graphite, Journal of Chemical Physics. Chem. Phys. 53 (1970) 1126–1130.
[31] F. Hofmann, D. Nguyen-Manh, M.R. Gilbert, C.E. Beck, J.K. Eliason, A.A. Maznev, W. Liu, D.E.J. Armstrong, K.A. Nelson, S.L. Dudarev, Lattice swelling and modulus change in a helium-implanted tungsten alloy: X-ray micro-diffraction, surface acoustic wave measurements, and multiscale modelling, Acta Mater. 89 (2015) 352–363.